CrystEngComm

Accepted Manuscript

ROYAL SOCIETY OF CHEMISTRY

www.rsc.org/crystengcomm

Journal Name

RSCPublishing

ARTICLE

Hollow structured and flower-like C@$MnCo_2O_4$ composite for high electrochemical performance in supercapacitor

Cite this: DOI: 10.1039/x0xx00000x

Received 00th January 2012,
Accepted 00th January 2012

DOI: 10.1039/x0xx00000x

www.rsc.org/

Lei Li,[a] Fei He,[a] Shili Gai,[a] Shenghuan Zhang,[a] Peng Gao,*[a] Milin Zhang,[a] Yujin Chen,*[b] and Piaoping Yang*[a]

Binary metal oxides $MnCo_2O_4$ nanosheets wrapped on hollow activated carbon shell (C@$MnCo_2O_4$) has been successfully synthesized through a facile hydrothermal method followed by a calcination process. The novel structure of flower-like C@$MnCo_2O_4$ composite, which consists good conductive carbon shell and well interconnected nanosheets, can efficiently facilitate the electrolyte penetration and offer expedite transport path for ion and electron. Notably, the large surface of the hybrid composite (347 m^2 g^{-1}) can endow large amount of active sites, which evidently accommodates the strain during cycling. Benefited from this elegant combination and the effectively mesoporous structure, the specific capacitance of the C@$MnCo_2O_4$ composite can be achieved as high as 728.4 F g^{-1}, which is, to the best of our knowledge, the highest value so far reported for $MnCo_2O_4$ based electrode materials. In addition, C@$MnCo_2O_4$ composite exhibits enhanced rate capability and an excellent cycling stability of 95.9 % retention after 1000 cycles at high current density of 8 A g^{-1}. Therefore, the desirable integrated electrical performance enables it to be a promising electrode material for supercapacitor application.

1. Introduction

With the continuous growth of demand for energy and ever-increasing environmental problem, there is an urgent need to develop some new types of efficient, clean and sustainable energy storage. Supercapacitors with high energy density, low maintenance and long cycle life are crucial supplements to be major power source for meeting the energy demands and increasing environmental concerns.[1–8] On account of the decisive role of electrode materials playing in the performance of supercapacitors, many efforts have been devoted to develop new electrode materials, aiming to achieve higher capacitance, longer cycle life and better rate performance.[9–13] Considering the charge storage mechanism of supercapacitors, three kinds can be determined: carbonaceous materials, metal oxides/ hydroxides, and conduction polymers.[14–16] Among all these three materials, transition metal oxides have aroused tremendous attention in the application of energy storage due to their fast redox kinetics and good reversibility, which can realize large pseudocapacitance and ideal stability.[17–21] Typical transition metal oxides such as NiO, Ru_2O, MnO_2, Co_3O_4 and Fe_3O_4 have been reported as electrode for supercapacitor.[21–24] However, there are still some immense demerits for those materials, pertinent to the use of expensive and toxic element (NiO, Ru_2O, Co_3O_4),[25–28] and low specific capacitance (MnO_2, Fe_3O_4).[16,29–31] Furthermore, the single component and morphology make them usually suffer from low utilization rate of the active materials and interior electron and ion transmission, leading to unsatisfactory specific capacitance and the rate performance of the supercapacitors. Hence, the electrode materials with mixed component and unique structure to overcome the demerits caused by single component are highly preferred.

Up to date, low-cobalt series, based on AB_2O_4 binary metal oxides with hierarchically complex structure, like $NiCo_2O_4$, $ZnCo_2O_4$ and $MnCo_2O_4$, have been extensively studied as promisingly alternative electrode materials for energy storage, due to their relatively low cost, high electrical performance and environmental benignity.[32–35] Nevertheless, the electrical research to $MnCo_2O_4$ composite, which is a typical representative among Co-based oxides, has been restricted because of the conflicting relationship between microstructure and electrochemical performance.[36–38] Besides, manganese oxides have a poor ionic conductivity and partial dissolution in alkaline electrolyte also leading to decay in capacitance. Despite some disappointing electrical properties of Mn element, we believe that $MnCo_2O_4$ can be exploited with considerable capacitance through some modification or combination with certain carbonaceous materials, which possesses both properties of lightweight and electronically conductivity.

Carbon-based materials, especially activated carbon shell, have been frequently employed in electrochemical capacitors for enhancing the ionic and electrical conductivities of the electrodes. Compared with other carbon materials like activated carbon powders or carbon nanotubes, porous activated carbon shell has fascinating features such as large surface area, excellent chemical stability and moderate production cost.[39–41]

It is worth noting that the advantages of high surface availability and pore volume of the porous carbon shell can not only efficiently deliver capacitance and power density, but also significantly increase the surface area of the electrode so as to allow more sites for charge storage, which brings about improved rate performance.[42–44] As a result, from the perspective of applications, it is highly desirable and attractive to synthesize electrode composites through the combination between activated carbon shell and $MnCo_2O_4$.

Inspired by the above analysis, we proposed a novel approach for producing hollow flower-like C@$MnCo_2O_4$ hybrid composite with the aid of the thermal decomposition of metal silicate and etching route. The activated carbon shell and nanosheets structured $MnCo_2O_4$ are simultaneously synthesized through calcination under a high-purity Ar procedure using resorcinol-formaldehyde resin and metal silicate as the precursors. Moreover, the hollow structured carbon shell plays a vital role in the preparation and the enhanced electrical performance of the composites. On one hand, it can provide support for anchoring the $MnCo_2O_4$ nanosheets. On other hand, hollow structure porous carbon can remarkably enhance the conductivity of the electrode material. Due to the unique material composition and structural features, the material exhibits high electrical performance when tested as an electrode for electrochemical evaluation in a three-electrode system at room temperature. It was found that the C@$MnCo_2O_4$ composites exert much higher specific capacitance than that of either pure porous carbon shell or pure $MnCo_2O_4$ nanosheets. Especially, high specific discharge capacitance of 728.4 F/g at a discharge current density of 1 A/g, good rate capability (71.3 % capacitance was retained at a large current density of 10 A/g) and excellent cycling stability (the capacitance maintains cycling stability of 95.9 % retention after 1000 cycles at a high charge/discharge current density of 8 A/g) have been achieved, suggesting that the hollow flower-like C@ $MnCo_2O_4$ materials are promising electrode material for supercapacitors. In addition, this novel route provides a facile approach for the fabrication of $MnCo_2O_4$ materials by using metal silicate as precursor, which can be potentially applied in the preparation of other AB_2O_4 binary metal oxides for supercapacitor application.

2. Experimental section

2.1. Preparation of samples

Preparation of SiO_2@RFs spheres: The silica spheres were fabricated *via* a classic Stöber method.[45] For the preparation of the SiO_2@RFs spheres, 0.4 g of silica spheres was ultrasonicated for 20 min in deionized water to form homogeneous solution, followed by slow addition of 0.2 g resorcinol, 2.5 g CTAB, 15 mL of ethanol and 0.1 mL of ammonia. The temperature was increased to 35 °C and maintained for 30 min under magnetic stirring. Then, 0.3 mL of a formaldehyde solution was added to the dispersion. After continuous stirring at 35 °C for 6 h, the precipitates were thoroughly washed with deionized water and ethanol before being dried at 60 °C for 12 h.

Preparation of RFs@metal silicate precursors: In a typical process for the synthesis of RFs@metal silicate precursors, 0.15 g of the as-prepared SiO_2@RFs was untrasonically dispersed in 10 mL of deionized water for 30 min. Meanwhile, 0.25 mmol of manganese chloride, 0.5 mmol cobalt nitrates and 10 mmol ammonia chlorides were dissolved in 20 mL of deionized water, and then 1 mL ammonia solution was added under vigorous stirring. Subsequently, the solution was mixed with the SiO_2@RFs suspension and transferred to autoclaves, kept at 140 °C for 10 h. After cooling down naturally, the brown sample was harvested by centrifugation and washed with water and ethanol several times.

Preparation of C@$MnCo_2O_4$ composites: For carbonization and the conversion from metal silicate to $MnCo_2O_4$, a certain amount of the as-prepared powder was loaded into a tube furnace and heated under high-purity Ar at 600 °C for 4 h. Black powder was obtained at room temperature and treated with a 2M NaOH solution to remove the silica cores. Finally, the resulting C@$MnCo_2O_4$ composites were separated by centrifugation, washed several times with deionized water and ethanol, and dried in vacuum at 60 °C for 12 h.

For comparison, pure carbon shell is synthesized by the calcination of SiO_2@RF**s** under high-purity Ar at 600 °C for 4 h and subsequent process of NaOH solution to remove SiO_2 spheres. And $MnCo_2O_4$ nanosheets were synthesized by the similar process of C@ $MnCo_2O_4$ mentioned above except the procedure of coating RFs (TEM images of pure carbon shell and $MnCo_2O_4$ nanosheets are provided in Fig. S1).

2.2. Materials characterization

X-ray diffraction (XRD) measurement was examined on a Rigaku D/max-TTR-III diffractometer using monochromatic Cu Kα radiation (λ = 0.15405 nm). Transmission electron microscopy (TEM) and high-resolution transmission electron microscopy (HRTEM) micrographs were performed on a FEI Tecnai G2 S-Twin transmission electron microscope with a field emission gun operating at 200 kV. The X-ray photoelectron spectra (XPS) were recording on a VG ESCALAB MK II electron energy spectrometer using Mg KR (1253.6 eV) as the X-ray excitation source. N_2 adsorption/desorption were measured at a liquid nitrogen temperature (77 K) using a Micromeritics Tristar 3020 instrument. The specific surface area was obtained by the Brunauer-Emmett-Teller (BET) method, and pore size distribution was calculated from the adsorption branch of the isotherm. All of the measurements were performed at room temperature.

2.3. Electrode preparation and electrochemical characterization

The working electrodes were prepared with the as-prepared active materials, acetylene black (AB), polytetrafluoroethylene (PTFE) in a weight ratio of 80:15:5. A small amount of absolute ethanol was then added to the mixture to promote the homogeneity, followed by 30 min of ultrasonicating. The as-obtained slurry was then pressed onto a Ni foam substrate and dried at 90 °C in vacuum for 4 h to remove the solvent. Finally, the as-formed electrodes were pressed at 10 Mpa. The electrolyte was a 6 M KOH aqueous solution. The electrochemical measurement was conducted in a three compartment using CHI666D electrochemical workstation. The reference electrode and counter electrode were Ag/AgCl and platinum, respectively. The specific capacitance can be estimated by the formula Csp = It/mV, where I is discharge current, t is the discharge time (s), V is the voltage change after a full charge and m is the mass of active material. Energy density (E) is calculated according to the following equation: $E= CspV^2/2$; Power density (P) is calculated according to the following equation: P= E/t.

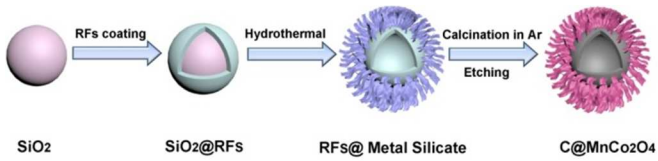

Scheme.1 Schematic illustration for the preparation of C@$MnCo_2O_4$ composite.

3. Results and discussion

3.1. Characterization of C@ $MnCo_2O_4$ composites

The synthetic procedure of hollow flower-like C@$MnCo_2O_4$ composite is shown in Scheme 1. Core-shell structured SiO_2@RFs is synthesized through a template-directed coating process using CTAB as surfactant. It should be noted that the self-assembly of CTAB and RF can really guarantee the uniform coating of carbon shell and the quantity of carbon source in the electrode materials, which can keep good morphology and enhance the electrical performance of the composite. In the reaction for the preparation of Mn (Co) silicate, silicate-ions groups dissolved from the colloidal silica can react with metal ions (Mn^{2+}, Co^{2+}) in alkaline condition and the composite has hollow structure due to the subsequent dissolution of SiO_2. The C@$MnCo_2O_4$@SiO_2 composite is then formed *via* the decomposition of silicate in high-purity Ar at high temperature. The ultimate $MnCo_2O_4$ can be formed by the equation: ((Mn-2Co) x (SiO_3) y) ⇔$MnCo_2O_4$+SiO_2. Finally, hollow structured C@$MnCo_2O_4$ is obtained by removal of SiO_2 adhered on the surface using NaOH solution. SiO_2 microspheres, which have a mean diameter of about 200 nm (Fig. 1A), were synthesized by a classic procedure of the well-know Stöber method. After being coated with a carbon-rich layer, as shown in Fig. 1B, core-shell SiO_2@RFs nanospheres with a thick RFs layer of about 30 nm are obtained.

To determine crystalline phase of C@ metal silicate,C@$MnCo_2O_4$@SiO_2, and C@$MnCo_2O_4$, we employed the XRD measurement and patterns of each composites are shown in Fig. 2. For metal silicate precursors, although the pattern is relative broad and overlapping, the diffraction can still be indexed to typical peaks of manganese silicate (JCPDS No. 12–0181) and cobalt silicate (JCPDS No. 29–0508) (The analysis of the XRD of the C@ metal silicate are provided in Fig. S2). After the deposition procedure in high temperature, the diffraction pattern of C@$MnCo_2O_4$@SiO_2 can be well

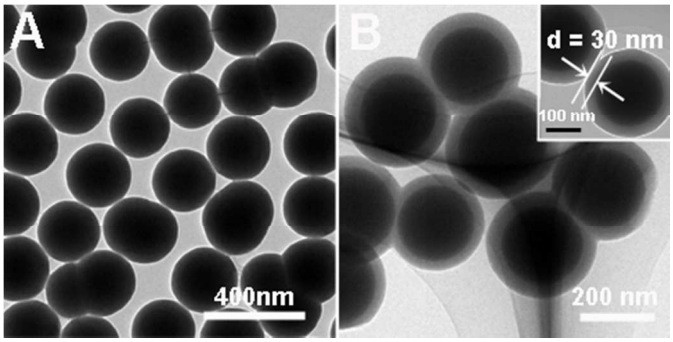

Fig. 1 TEM images of SiO_2 microspheres (A) and SiO_2@RFs spheres (B).

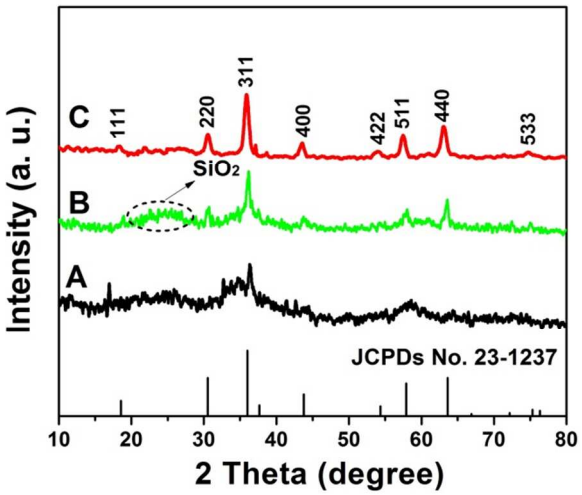

Fig. 2 XRD patterns of C@ metal silicate (A), C@$MnCo_2O_4$@SiO_2 (B), and C@$MnCo_2O_4$(C) composites.

indexed to cubic $MnCo_2O_4$ phase (JCPDS No. 23–1237) with a spinel structure, except for a weak broad peak around 22°, assigned to amorphous SiO_2. Compared with C@$MnCo_2O_4$ @SiO_2, the major diffractions of the C@$MnCo_2O_4$ composite are more clear, suggesting that the phase of cubic $MnCo_2O_4$ can be well maintained after etching process. In addition, the disappearance of the peak of amorphous SiO_2 confirms the removal of silica on the composite by NaOH solution. The XRD pattern of C@$MnCo_2O_4$ reveals that the structure of $MnCo_2O_4$ can be regarded as mixed valence oxide that adopts a cubic spinel structure in which manganese and cobalt are distributed over both octahedral and tetrahedral sites, which

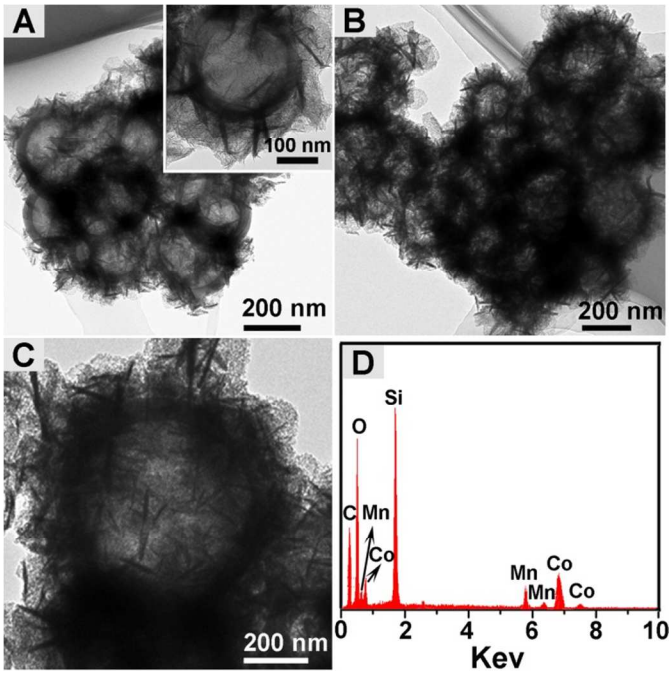

Fig. 3 TEM images of C@metal silicate (A), C@$MnCo_2O_4$@SiO_2 (B, C), and the corresponding EDS pattern (D).

are favorable for composite to exhibit a high capacitive performance..

In Fig. 3A, the C@metal silicate composites present hollow structure coated with flowerlike nanosheets, which is assigned to the formation of metal silicate by the reaction of silicate-ions groups dissolved from silica and metal ions under hydrothermal condition. The high-magnification image (inset in Fig. 3A) of an individual microsphere definitely confirms that the flower-like metal silicate is self-assembled by small nano-petals. After calcination under Ar, the obtained C@$MnCo_2O_4$@SiO_2 keeps the morphological properties of C@metal silicate except for the shrinkage of composite, which is ascribed to the decomposition of the precursor. In Fig. 3C, the weak contrast between carbon shell and nanosheets provides a visual evidence for the generation of $MnCo_2O_4$ and SiO_2. From the EDS pattern of C@$MnCo_2O_4$@SiO_2 (Fig. 3D), we can affirm the existence of C, O, Si, Mn, Co. Besides, the atomic ratio of Mn/Co is about 1:2, which can further indicate the formation of $MnCo_2O_4$.

The morphology and nanostructure of the etched product are investigated by TEM analysis. The low-magnified TEM image in Fig. 4A verifies that the C@$MnCo_2O_4$ sample is comprised of numerous flower-like $MnCo_2O_4$ nanopetals, which maintains the well-preserved hierarchical structure with diameter of 400-500 nm. The selected area electron diffraction (SAED) pattern exhibits the polycrystalline nature of the $MnCo_2O_4$, and the diffraction rings can be agree with the XRD patterns. The typical structure of C@MnCo2O4 is shown in the magnified TEM image in Fig. 4B and the thickness of the carbon is about 20 nm. More details of C@$MnCo_2O_4$ composite can be found in Fig. 4C, which reveals that the exterior of each flower-like $MnCo_2O_4$ possesses abundant, randomly assembled, irregular-shaped nanosheets/flakes. This unique structure of $MnCo_2O_4$ composite can tremendously increase the external surface of the composite so as to provide plenty of electrical contact with the current collector, which is necessary for improved electrochemical capacity and higher charge transfer kinetics. In addition, the thickness of the inner carbon shell decreases from 30 nm to 20 nm, better demonstrating the conversion and carbonization from RFs to activated carbon shell. Notably, the distinction between carbon shell and $MnCo_2O_4$ is much clearer than that of C@$MnCo_2O_4$@SiO_2, which can be ascribed to the removal of SiO_2 by NaOH solution. More importantly, the collaborative effect of carbon shell and $MnCo_2O_4$ can directly enhance the energy

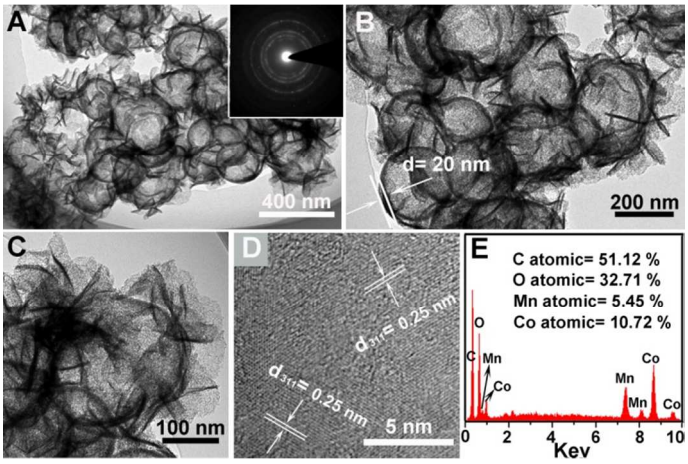

Fig. 4 Low-magnified (A), high-magnified (B, C) TEM images, HRTEM image (D), and EDS pattern (E) of C@MnCo2O4. Inset in panel B is the SAED pattern.

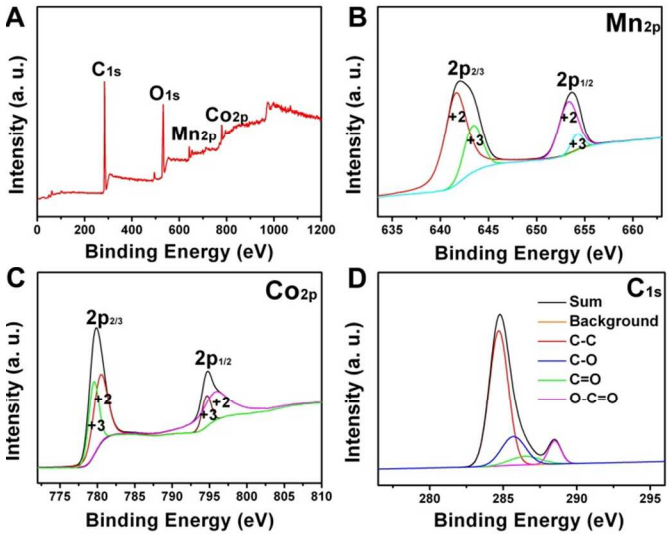

Fig. 5 XPS spectra of C@$MnCo_2O_4$ composite: survey spectrum (A), Mn2p (B), Co2p (C) and C1s (D).

storage performance due to the elimination of SiO_2. In the HRTEM image of the C@ $MnCo_2O_4$ composites (Fig. 4D), the measured lattice is 0.25 nm, matching well with the (311) plane of cubic-phased $MnCo_2O_4$. The analysis result of EDS is displayed in Fig. 4E. It is seen that the sample contains four elements (C, O, Mn and Co). The increasing content of carbon and the disappearance of Si element are assigned to the etching of SiO_2, which is consistent with the TEM result. Moreover, the atomic ratio of Mn/Co (1:2) remains the same as C@$MnCo_2O_4$@SiO_2, which further conform the existence of $MnCo_2O_4$ and manifest that $MnCo_2O_4$ keeps stable after etching treatment.

The information about the chemical element valence of C@$MnCo_2O_4$ composite was investigated by X-ray photoelectron spectroscopy (XPS). A wide survey scan of XPS spectra is taken in the range 0-1200 eV, as shown in Fig. 5A. No extra peak related with any impurities other than C, O, Mn and Co can be detected. In Mn2p spectrum (Fig. 5B), two kinds of manganese species are detected and attributed to species containing Mn^{2+} and Mn^{3+} ions. Specially, the fitting peaks at binding energies of 641.5 and 653.4 eV are assigned to Mn^{2+}, while the peaks at 643.5 and 654.5 eV are ascribed to the existence of Mn^{3+}. Similarly, the Co2p spectrum is best fitted considering two spin-orbit doublets characteristic of Co^{2+} and Co^{3+}, which can be observed at 780.4 and 795.7 eV, respectively. Accordingly, it is anticipant that this binary solid state redox couple Mn^{3+}/Mn^{2+} and Co^{3+}/Co^{2+} in the $MnCo_2O_4$ structure can provide plenty of electroactive sites, which may be a fatal factor contributing to the electrical performance the $MnCo_2O_4$ composites electrode.[35] In Fig. 5D, deconvolution of the C1s peak shows the presence of non-oxygenated carbon species at 284.8 eV, which can further attest the carbonization from RFs to activated carbon shell that can be helpful for the conductivity of the active material. With the good combination of activated carbon shell and $MnCo_2O_4$, the C@$MnCo_2O_4$ composite should exhibit high cycle performance and a good rate capability, due to the synthetic effect between the activated carbon shell and $MnCo_2O_4$ composite.

It is well known that the specific surface areas and pore-size distribution are dominant parameters closely related to the

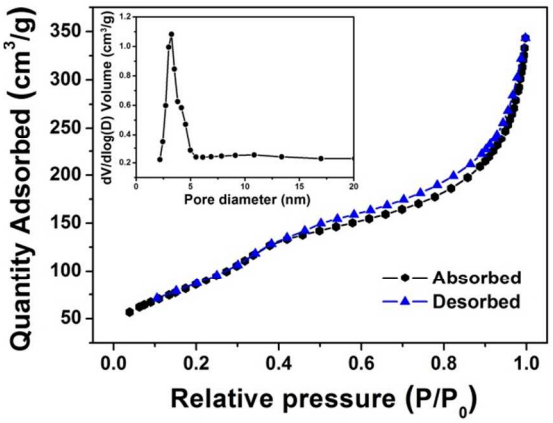

Fig. 6 N_2 sorption isotherm and pore size distribution (inset) of C@$MnCo_2O_4$ composite.

specific capacitance of electrode materials.[46–49] Therefore, the as-prepared C@$MnCo_2O_4$ was further characterized for the specific area and porosity by nitrogen adsorption and desorption experiment. As shown in Fig. 6, the curve exhibits the prominent feature of type-IV isotherm with a distinct hysteresis loop of H_2 in the P/P_0 range of 0.4-1.0 nm, suggesting the existence of the disordered mesopore. The obtained pore size distribution is narrow and centered at around the diameter of 3.5 nm, further confirming the presence of mesopore. It is well-established that the pore size of the electrode material within 2-5 nm is optimal for the behavior of supercapacitors, which is beneficial to the transport and diffusion of ions since the nanoscale pores can facilitate the penetration of electrolyte and ions through bulky electrodes.[50, 51] The as-prepared C@$MnCo_2O_4$ composite presents a high BET surface area of 347.4 m^2 g^{-1}, which can provide the effective contact areas of active materials and electrolyte.

To certify the electrochemical superiority for the combination between activated carbon shell and $MnCo_2O_4$, a comparative cyclic voltammetry measurement has been carried out for activated carbon shell, pure $MnCo_2O_4$ and C@$MnCo_2O_4$ composite at a 5 mV s^{-1} using 6 M KOH electrolyte. As shown in Fig. 7A, well-defined redox peaks are visible in these three voltammograms in a potential window of 0 to 0.52 V, indicating that electrochemical capacitance is mainly ascribed to Faradaic redox mechanism.[52–54] Obviously, for the curve of pure $MnCo_2O_4$ composite, intense peaks located at 0.25 V (corresponding cathodic peak at 0.4 V) and a relative weak appeared at 0.2 V (corresponding cathodic peak at 0.35 V) can be assigned to the transition of the redox couple M-O and M-O-OH (M represents Mn and Co) in an alkaline electrolyte. Notably, the flower-like $MnCo_2O_4$ can offer multiple functions: it is not only an excellent capacitor itself, but also an electron and ion permeating high-way, serving a large specific area for electrolyte into the entire structure.[55] For the C@$MnCo_2O_4$ composite, a similar phenomenon can be observed, while the two cathodic peaks are more apparent and the integrated CV area is significantly larger, which are attributed to the synergistic effect between activated carbon shell and $MnCo_2O_4$. This affirms that the C@$MnCo_2O_4$ based electrode is an ideal choice for pseudocapacitive devices. To further evaluate the potential application of C@$MnCo_2O_4$ material acting as electrode for supercapacitor, the CV measurements with various scan rates between 5 and 50mV s^{-1} are performed in 6 M KOH aqueous electrolyte. As shown in Fig. 7B, the shape of

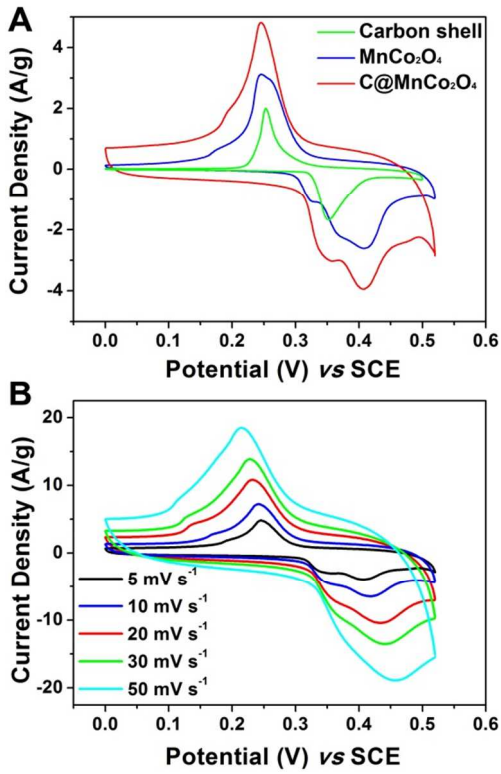

Fig. 7 CV curves of carbon shell, pure $MnCo_2O_4$ and C@$MnCo_2O_4$ composite at a rate of 5 mV s^{-1} (A), and CV curves of C@$MnCo_2O_4$ measured at scan rates from 5-50 mV s^{-1} (B).

CV curves has unapparent distortions by increasing the scan rate, illustrating the unique structure of C@$MnCo_2O_4$ is beneficial to fast electron transport and change separation. Furthermore, with the increase of the scan rates, the CV curves of C@$MnCo_2O_4$ have wider separation between the anodic and cathodic peaks, revealing higher power character and better electrochemical reversibility of C@$MnCo_2O_4$ electrode, which may result from the participation of activated carbon shell that induces the considerable broadening of some redox.

Galvanostatic charge-discharge test is a complementary method for determining the specific capacitance of electrode materials under constant condition. Charging-discharging curves of each sample at a current density of 1 A g^{-1} in a potential range of 0-0.5 V are shown Fig. 8A. The voltage plateaus match well with the peaks displayed in the CV curve, which confirms the pseudocapacitance character of each sample. And the discharge curve of C@$MnCo_2O_4$ exhibits two different stages rather than a straight line, also suggesting the faradic reaction has taken place. Evidently, the C@$MnCo_2O_4$ composite delivers a much higher capacitance than those of activated carbon shell and pure $MnCo_2O_4$. According to the formula mentioned in section 2.3, the corresponding specific capacitance is 728.4, 420.2, and 170.7 F g^{-1} for C@$MnCo_2O_4$, pure $MnCo_2O_4$, activated carbon shell, which is in good agreement with the analysis of CV curves that C@ $MnCo_2O_4$ owns best electrochemical properties.

Rate capability is a key parameter for assessing the performance of electrochemical capacitors in application of supercapacitor.[49, 53, 56, 57] The representative galvanostatic charge-discharge plots of voltage versus time for C@$MnCo_2O_4$ composite at various current densities(1, 2, 3, 5, 8, and 10 A g^{-1})

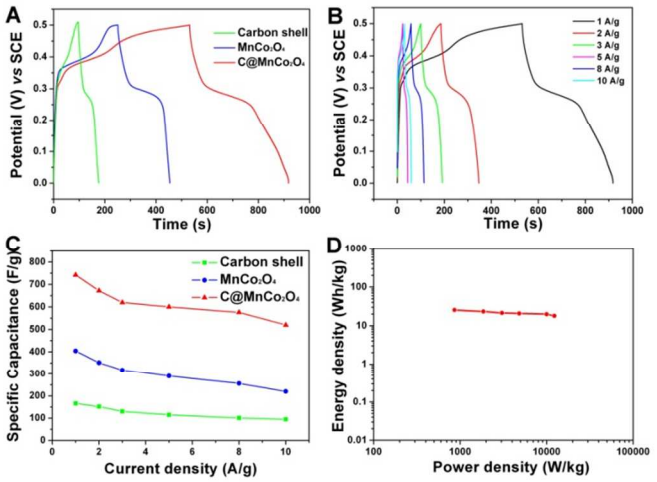

Fig. 8 Galvanostatic (GV) discharge curves of carbon shell, pure $MnCo_2O_4$ and $C@MnCo_2O_4$ composite (A), discharge curves of $C@MnCo_2O_4$ composite measured at various discharge current (B), current density dependence of the specific capacitance (C) for carbon shell, pure $MnCo_2O_4$ and $C@MnCo_2O_4$ composite, and Ragone plot of $C@MnCo_2O_4$ composite.

are displayed in Fig. 8B (Charge-discharge plots of pure carbon shell and $MnCo_2O_4$ are provided in Fig S3). The discharge time decreases monotonically with the increasing current density, which can be attributed to the redox reaction moving progressively to keep the pace with fast potential. The typical data of the specific capacitance for each sample at controlled current densities are shown in Fig. 8C for comparison, which are calculated based on discharge curves. Similarly, $C@MnCo_2O_4$ composite exhibits a much higher capacitance than those of single component electrode at all current densities. The improvement in specific capacitance is mainly ascribed to the unique structure of $C@MnCo_2O_4$ with large surface area and electrically conductive networks, which can provide more active centers and facilitate contact with the electrolyte ions (OH^-). At a high current density of 10 A g^{-1}, the capacitance maintains 71.3% (from 728.4 to 519 F g^{-1}), indicating that the $C@MnCo_2O_4$ possesses an excellent rate capability, which is fatal for electrode materials to achieve both high power and energy densities. Based on the electrical data, Ragone plot of $C@MnCo_2O_4$ composite, indicating the relation between energy density and power density, is calculated and shown in Fig 8D. The energy density of the $C@MnCo_2O_4$ can be estimated to be 25.50 Wh/kg at a power density of 856.07 W/kg. And the energy density is still as high as 19.01 Wh/kg at a power density of 12326.79 W/kg, indicating the excellent utility of the ternary composite as electrode material at high current.

To further elucidate the origin of the high electrochemical performance for $C@MnCo_2O_4$ composite, electrochemical impedance spectrum (EIS) was performed to examine the synergistic effect of activated carbon shell and $MnCo_2O_4$. Fig. 9 depicts the EIS of carbon shell, pure $MnCo_2O_4$ and $C@MnCo_2O_4$ composite (insets are the semicircle in high frequency). The plots for each electrode materials are similar and composed of one semicircle at higher frequency followed by a straight line along the imaginary axis at lower frequency, which indicates typical capacitor behave.[57–59]The linear part corresponds to the Warburg impedance (W), which manifests diffusive impedance of the OH^- within electrode.[60-63] We can observe that the curve of $C@MnCo_2O_4$ composite contains a

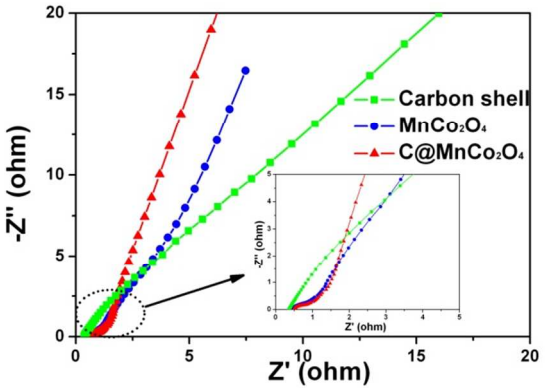

Fig. 9 Nyquist plots of the EIS (D) for carbon shell, pure $MnCo_2O_4$ and $C@MnCo_2O_4$ composite.

more vertical slope which demonstrates more facile electrolyte diffusion to the surface of the sample and high reactivity compared with other samples. In addition, the semicircle of the Nyquist graph signifies the Faradic reactions and the corresponding diameter represents the interfacial resistivity. The diagram for the $C@MnCo_2O_4$ composite contains a much smaller semicircle than that of pure $MnCo_2O_4$, suggesting the better intrinsic conductivity of $C@MnCo_2O_4$ composite. The smaller charge transfer resistance benefits from the elegant combination between activated carbon shell and flower-like $MnCo_2O_4$, which can be conducive to the fast ions/electrons transfer within the active material and electrolyte. Thus, the unique structure of $C@MnCo_2O_4$ composite with high surface area and porous network can really contribute to enhanced electrochemical performance.

As the cycling stability of electrode material is critical for practical application, the flower-like $C@MnCo_2O_4$ composites were examined at a charge-discharge current density of 8 A g^{-1} in the potential range of 0 to 5V for 1000 respective cycles. As shown in Fig. 10, interestingly, instead of decrease, the specific capacitance increases gradually during the initial 250 cycles, which may be attributed to the active material that can be activated to providemore available active centers and allow the trapped ions to diffuse out by parcels. After 1000 cycles, the $C@MnCo_2O_4$ exhibits an excellent retention of 95.9 %, revealing that the $C@MnCo_2O_4$ composite owns desirable long-

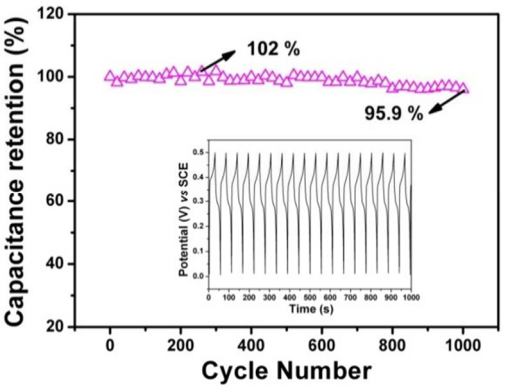

Fig. 10 Cycling performance of $C@MnCo_2O_4$composite measured at 8 A/g with a voltage window of 0–0.5 V.

term electrochemical stability even under high current density. There are several factors attributable to the excellent cycling stability of the C@$MnCo_2O_4$ composite. First, the hollow structure of the activated carbon shell with good electrical conductivity after calcination treatment can enable the full exposure of the active area to the electrode, enhancing the utilization of the materials. Second, the flower-shaped $MnCo_2O_4$ composite synthesized by the hydrothermal and annealing processes is well wrapped on the surface of the carbon shell. It could offer large conductive matric for the electron transport during the Faradic reaction, which is beneficial for maintaining electronic and ionic conductivities, therefore achieving high specific capacity and life-cycle durability.

Conclusions

In summary, we have employed a new strategy to prepare flower-like C@$MnCo_2O_4$ hybrid composite using a facile hydrothermal method combined with a post calcination process. Due to the unique hollow structure, high specific surface area, suitable pore channel, the C@$MnCo_2O_4$ composite exhibits high specific capacitance, low charge-transfer resistance, superior capacitance retention. A high specific capacitance of 728.4 F g^{-1} has been achieved at a current density of 1A g^{-1} and 95.9 % of the initial capacitance is retained after 1000 cycles. This novel synthetic route provides a promising design towards other metal oxide materials for future supercapacitor application.

Acknowledgements

This work was supported by funding from financial supports from the National Natural Science Foundation of China (NSFC 21271053, 51472058, 21401032), Research Fund for the Doctoral Program of Higher Education of China (20112304110021), Natural Science Foundation of Heilongjiang Province (LC2012C10), Harbin Sci.-Tech. Innovation Foundation (RC2012XK017012), Fundamental Research Funds for the Central Universities of China.

Notes and references

a Key Laboratory of Superlight Materials and Surface Technology, Ministry of Education, College of Material Science and Chemical Engineering, Harbin Engineering University, Harbin 150001, P. R. China. E-mail: yangpiaoping@hrbeu.edu.cn; gaopeng@hrbeu.edu.cn
b College of Sciences, Harbin Engineering University, Harbin 150001, P. R. China.
E-mail: chenyujin@hrbeu.edu.cn

1 S. Chen, J. W. Zhu and X. Wang, *J. Phys. Chem. C*, 2010, **114**, 11829–11834.
2 X. Feng, Y. Liang, L. Zhi, A. Thomas, D. Wu, I. Lieberwirth, U. Kolb and K. Müllen, *Adv. Funct. Mater.*, 2009, **19**, 2125–2129.
3 M. He, F. Qiu and Z. Q. Lin, *Energy Environ. Sci*, 2013, **6**, 1352–1361.
4 Y. Zhang, W. W. Zhou, Z. Jin, L. Ding, Z. Y. Zhang, X. I. Liang and Y. Li, *Chem. Mater.*, 2008, **20**, 7521–7525.
5 C. W. Sun, F. Li, C. Ma, Y. Wang, Y. L. Ren, W. Yang, Z. H. Ma, J. Q. Li, Y. J. Chen, Y. Kim and L. Q. Chen, *J. Mater. Chem. A*, 2014, **2**, 7188–7196.
6 B. Y. Xia, H. B. Wu, Y. Yan, X. W. Lou and X. Wang, *J. Am. Chem. Soc.*, 2013, **135**, 9480–9485.
7 Zang. X, Chen. Q, Li. P, He. Y, Li. X, Zhu. M, Li. X, Wang. K, Zhong. M, Wu. D. and Zhu. H, *Small*, 2014, **10**, 2583–2588.
8 G. A. Snook, P. Kao and A. S. Best, *J. Power Sources*, 2011, **196**, 1–12.
9 J. Li, J. Wang, X. Liang, Z. Zhang, H. Liu, Y. Qian and S. Xiong, *ACS Appl. Mat. Interfaces*, 2014, **6**, 24-30.
10 Y. P. Zhai, Y. Q. Dou, D. Y. Zhao, P. F. Fulvio, R. T. Mayes and S. Dai, *Adv. Mater.*, 2011, **23**, 4828–4850.
11 G. X. Wang, H. Liu, J. Liu, S. Z. Qiao, G. Q. M. Lu, P. Munroe and H. Ahn, *Adv. Mater*, 2010, **22**, 4944–4948.
12 G. A. Snook, T. L. Greaves and A. S. Best, *J. Mater. Chem.*, 2011, **21**, 7622-7629.
13 Y. N. Meng, Y. Zhao, C. G. Hu, H. H. Cheng, Y. Hu, Z. P. Zhang, G. Q. Shi and L. T. Qu, *Adv. Mater*, 2013, **25**, 2326-2331.
14 Z. S. Wu, Y. Sun, Y. Z. Tan, S. Yang, X. Feng and K. Mullen, *J. Am. Chem. Soc*, 2012, **134**, 19532–19535.
15 W. Han, M. He, M. Byun, B. Li and Z. Q. Lin, *Angew. Chem. Int. Ed.*, 2013, **52**, 2564-2568.
16 L. Ding, A. Tselev, J. Y. Wang, D. N. Yuan, H. B. Chu, T. P. McNicholas, Y. Li and J. Liu, *Nano Lett.*, 2009, **9**, 800-805.
17 S. Chabi, C. Peng, D. Hu and Y. Q. Zhu, *Adv. Mater.*, 2014, **26**, 2440–2445.
18 Z. L. Zhang, Q. Q. Tan, Y. F. Chen, J. Yang and F. B. Su, *J. Mater. Chem. A*, 2014, **2**, 5041–5050.
19 C. Yu, J. Yang, C. T. Zhao, X. M. Fan, G. Wang and J. S. Qiu, *Nanoscale*, 2014, **6**, 3097–3104.
20 J. W. Zhu, S. Chen, H. Zhou and X. Wang, *Nano Res.*, 2012, **5**, 11-19.
21 H. Liu, G. X. Wang, J. Liu, S. Z. Qiao and H. J. Ahn, *J. Mater. Chem.*, 2011, **21**, 3046–3052.
22 Y. C. Cao, M. Zhu, P. X. Li, R. J. Zhang, X. M. Li, Q. M. Gong, K. L. Wang, M. L. Zhong, D. H. Wu, F. Lin and H. W. Zhu, *Phys. Chem. Chem. Phys.*, 2013, **15**, 19550–19556.
23 J. Duay, S. A. Sherrill, Z. Gui, E. Gillette and S. B. Lee, *ACS Nano*, 2013, **7**, 1200–1214.
24 K. Pinkert, L. Giebeler, M. Herklotz, S. Oswald, J. Thomas, A. Meier, L. Borchardt, S. Kaskel, H. Ehrenberg and J. Eckert, *J. Mater. Chem. A*, 2013, **1**, 4904–4910.
25 C. Z. Yuan, X. G. Zhang, L. H. Su, B. Gao and L. F. Shen, *J. Mater. Chem.*, 2009, **19**, 5772–5777.
26 H. L. Wang, H. S. Casalongue, Y. Y. Liang and H. J. Dai, *J. Am. Chem. Soc*, 2010, **132**, 7472–7477.
27 Y. Zhao, J. Liu, Y. Hu, H. H. Cheng, C. G. Hu, C. C. Jiang, L. Jiang, A. Y. Cao and L. T. Qu, *Adv. Mater*, 2013, 25, 591–595.
28 J. H. Jiang, W. D. Shi, S. Y. Song, Q. L. Hao, W. Q. Fan, X. F. Xia, X. Zhang, Q. Wang, C. B. Liu and D. Yan, *J. Power Sources*, 2014, **248**, 1281–1289.
29 R. Li, X. Ren, F. Zhang, C. Du and J. Liu, *Chem. Commun.*, 2012, **48**, 5010–5012.
30 J. Liu, S. Liu, S. Zhuang, X. Wang and F. Tu, *Ionics*, 2013, **19**, 1255–1261.
31 Y. Xiao, Y. Cao, Y. Gong, A. Zhang, J. Zhao, S. Fang, D. Jia and F. Li, *J. Power Sources*, 2014, **246**, 926–933.

32 A. Pendashteh, M. S. Rahmanifar, R. B. Kaner and M. F. Mousavi, *Chem. Commun.*, 2014, **50**, 1972–1975.
33 C. Fu, G. Li, D. Luo, X. Huang, J. Zheng and L. Li, *ACS Appl. Mat. Interfaces*, 2014, **6**, 2439–2449.
34 F. Deng, L. Yu, G. Cheng, T. Lin, M. Sun, F. Ye and Y. Li, *J. Power Sources*, 2014, **251**, 202-207.
35 X. Li, X. B. Zang, Z. Li, X. M. Li, P. X. Li, P. Z. Sun, X. Lee, R. J. Zhang, Z. H. Huang, K. L. Wang, D. H. Wu, F. Y. Kang and H. W. Zhu, *Adv. Funct. Mater.*, 2013, **23**, 4862-4869.
36 D. Yang, *J. Power Sources*, 2012, **198**, 416-422.
37 W. Y. Li, K. B. Xu, G. S. Song, X. Y. Zhou, R. J. Zou, J. M. Yang, Z. G. Chen and J. Q. Hu, *CrystEngComm*, 2014, **16**, 2335–2339.
38 L. Li, Y. Q. Zhang, X. Y. Liu, S. J. Shi, X. Y. Zhao, H. Zhang, X. Ge, G. F. Cai, C. D. Gu, X. L. Wang and J. P. Tu, *Electrochim. Acta*, 2014, **116**, 467–474.
39 Y. Shim and H. J. Kim, *ACS Nano*, 2010, **4**, 2345–2355.
40 L. Wang, Y. Yu, P. C. Chen, D. W. Zhang and C. H. Chen, *J. Power Sources*, 2008, **183**, 717–723.
41 Y. W. Zhu, S. Murali, M. D. Stoller, K. J. Ganesh, W. W. Cai, P. J. Ferreira, A. Pirkle, R. M. Wallace, K. A. Cychosz, M. Thommes, D. Su, E. A. Stach and R. S. Ruoff, Science, 2011, **332**, 1537–1541.
42 Z. B. Lei, N. Christov and X. S. Zhao, *Energy Environ. Sci.*, 2011, **4**, 1866–1873.
43 S. Bose, T. Kuila, A. K. Mishra, R. Rajasekar, N. H. Kim and J. H. Lee, *J. Mater. Chem.*, 2012, **22**, 767–784.
44 M. Arulepp, J. Leis, M. Latt, F. Miller, K. Rumma, E. Lust and A. F. Burke, *J. Power Sources*, 2006, **162**, 1460–1466.
45 B. Guan, X. Wang, Y. Xiao, Y. Liu and Q. Huo, *Nanoscale*, 2013, **5**, 2469–2475.
46 Q. Lu and Y. Zhou, *J. Power Sources*, 2011, **196**, 4088–4094.
47 C. Liu, F. Li, L. P. Ma and H. M. Cheng, *Adv. Mater.*, 2010, **22**, E28.
48 S. H. Xuan, F. Wang, X. L. Gong, S. K. Kong, J. C. Yu and K. C. F. Leung, *Chem. Commun.*, 2011, **47**, 2514–2516.
49 G. P. Wang, L. Zhang and J. J. Zhang, *Chem. Soc. Rev.*, 2012, **41**, 797–828.
50 B. Wang, Q. Liu, Z. Y. Qian, X. F. Zhang, J. Wang, Z. S. Li, H. J. Yan, Z. Gao, F. B. Zhao and L. H. Liu, *J. Power Sources*, 2014, **246**, 747–753.
51 W. Zhang, C. Ma, J. Fang, J. Cheng, X. Zhang, S. Dong and L. Zhang, *RSC Adv.*, 2013, **3**, 2483–2490.
52 L. Yu, L. Zhang, H. B. Wu, G. Q. Zhang and X. W. Lou, L. Yu, L. Zhang, H. B. Wu, G. Q. Zhang and X. W. Lou, *E Energy Environ. Sci,*, 2013, **6**, 2664-2671.
53 M. C. Liu, L. B. Kong, C. Lu, X. M. Li, Y. C. Luo and L. Kang, *ACS Appl. Mater. Interfaces*, 2012, **4**, 4631–4636.
54 X. Wang, X. Han, M. Lim, N. Singh, C. L. Gan, M. Jan and P. S. Lee, *J. Phys. Chem. C*, 2012, **116**, 12448–12454.
55 X. Y. Yu, X. Z. Yao, T. Luo, Y. Jia, J. H. Liu and X. J. Huang, *ACS Appl. Mater. Interfaces*, 2014, **6**, 3689–3695.
56 J. Gomez and E. E. Kalu, *J. Power Sources*, 2013, **230**, 218–224.
57 J. Xiao, L. Wan, S. Yang, F. Xiao and S. Wang, *Nano Lett.*, 2014, **14**, 831–838.
58 N. Du, H. Zhang, B. Chen, J. B. Wu, X. Y. Ma, Z. H. Liu, Y. Q. Zhang, D. Yang, X. H. Huang and J. P. Tu, *Adv. Mater.*, 2007, **19**, 4505–4509.
59 W. Y. Li, K. B. Xu, G. S. Song, X. Y. Zhou, R. J. Zou, J. M. Yang, Z. G. Chen and J. Q. Hu, *Crystengcomm*, 2014, **16**, 2335-2339.
60 R. Ding, L. Qi, M. J. Jia and H. Y. Wang, *J. Power Sources*, 2014, **251**, 287–295.
61 L. Wang, H. Ji, S. Wang, L. Kong, X. Jiang and G. Yang, *Nanoscale*, 2013, **5**, 3793–3799.
62 L. Wei, M. Sevilla, A. B. Fuertes, R. Mokaya and G. Yushin, *Adv. Funct. Mater.*, 2012, **22**, 827–834.
63 L. Li, Y. Q. Zhang, X. Y. Liu, S. J. Shi, X. Y. Zhao, H. Zhang, X. Ge, G. F. Cai, C. D. Gu, X. L. Wang and J. P. Tu, *Electrochim. Acta*, 2014, **116**, 467-474.
64 N. Handa, T. Sugimoto, M. Yamagata, M. Kikuta, M. Kono and M. Ishikawa, *J. Power Sources*, 2008, **185**, 1585–1588.